

# **Ocean coupling controls rupture velocity of fastest observed ice shelf rift propagation event**

**Stephanie D. Olinger<sup>1,2</sup>, Bradley P. Lipovsky<sup>2</sup>, Marine A. Denolle<sup>2</sup>**

<sup>1</sup>Department of Earth and Planetary Sciences, Harvard University; Cambridge, Massachusetts, USA.

<sup>2</sup>Department of Earth and Space Sciences, University of Washington; Seattle, Washington, USA.

Corresponding author. Stephanie Olinger ([stepholinger@fas.harvard.edu](mailto:stepholinger@fas.harvard.edu))

## **Key Points:**

- We observe rift propagation faster than 10 m/s, suggesting that rifting presents a mechanism of rapid ice shelf change or collapse.
- Rift fracture mechanics and fluid flow in the subshelf cavity act in concert to control the precise speed of rift propagation.
- Rapid rifting induces mixing in the subshelf cavity comparable in magnitude to mixing induced by calving from marine terminating glaciers.

## Abstract

The Antarctic ice sheet is buttressed by floating ice shelves that calve icebergs along large fractures called rifts. We report the first-ever seismic recording of a multiple-kilometer rift propagation event located in Pine Island Glacier Ice Shelf. The rift grew 10.5 km at a speed of 34.8 m/s, the fastest known ice fracture at this scale. We simulate ocean-coupled rift propagation and find that hydrodynamics control rupture velocities. During rift propagation, ocean water flows into the rift at a rate of at least 2300 m<sup>3</sup>/s and causes mixing in the subshelf cavity. Our observations support the hypotheses that large ice shelf rift propagation events are brittle, hydrodynamically limited, and exhibit sensitive coupling with the surrounding ocean.

## Plain Language Summary

The flow rate of glaciers in Antarctica is regulated by floating bodies of ice called ice shelves. Ice shelves contain huge cracks called rifts that extend for many kilometers. On many ice shelves, these rifts grow until they disconnect a large iceberg from the rest of the ice shelf. In this study, we use satellite data and seismic recordings to observe over 10 km of rift growth at Pine Island Glacier, an important glacier in West Antarctica. The rift growth event we report is the fastest instance of rift growth ever observed. Using a computer simulation, we model the rift growth process. We find that the ice shelf interacts with the ocean as it cracks, and this interaction determines how quickly rifts can grow. Our observations and simulation also suggest that rift growth causes mixing in the ocean underneath the floating ice shelf.

## 1 Introduction

The possibility of rapid ice mass loss from the West Antarctic ice sheet has remained contentious for over forty years (Hughes et al., 1981). The seminal collapse of the Larsen B ice shelf provided incontrovertible evidence linking ice shelf fracturing to rapid ice mass loss (Scambos et al., 2004), with more recent work emphasizing spatial variability in ice shelf vulnerability (Fürst et al., 2016; Lai et al., 2020; Reese et al., 2018) and pervasive damage (Borstad et al., 2012; Lhermitte et al., 2020). In contrast to such progress in understanding large-scale dynamics, the detailed nature of the fracturing processes that may (or may not) contribute to rapid ice mass loss has remained controversial. Significant research foci include hydrofracture, a process that is clearly implicated in ice shelf collapse (Banwell et al., 2013; Lai et al., 2020; Robel & Banwell, 2019), and the marine ice-cliff instability (Bassis et al., 2021), a process by which rapid ice mass loss is hypothesized to occur (DeConto & Pollard, 2016) and whose validity has been critically examined on observational (Pattyn et al., 2018) and theoretical (Clerc et al., 2019) grounds. Yet among all ice shelf fracture processes, rift propagation is the mechanism by which the largest calved icebergs are created, i.e., icebergs with areal extent ranging from 1 km<sup>2</sup> to 1x10<sup>4</sup> km<sup>2</sup> (Greene et al., 2022). Although calving due to rift propagation is generally thought of as a natural cyclic process on decadal timescales (Greene et al., 2022), recent studies have examined the deterioration of this natural cycle (Arndt et al., 2018) and associated increases in ice mass loss (Joughin et al., 2021). Given the enormous scale of tabular iceberg calving, it is therefore important to better understand the rift propagation process in order to understand whether deviations from the natural rifting-calving cycle are a harbinger of Antarctic ice shelf dynamics in a warming climate.

Rifting remains a challenging physical process to observe. Many rifts in Antarctica's largest ice shelves, like Ross Ice Shelf, appear to be stable on decadal timescales with minimal propagation in the observational record (Walker et al., 2013). In contrast, rifts on highly dynamic ice shelves like Pine Island Glacier initiate, propagate, and calve icebergs every few years (Jeong et al., 2016, Olinger et al., 2019; Walker et al., 2013). While remote sensing provides an accurate and effective method of measuring many aspects of ice shelf evolution, the wide range of rift propagation timescales prevents the full spectrum of rift behavior from being observed by remote sensing alone. Because the interval between most satellite instruments is several days, rift propagation on timescales of seconds to hours is inherently aliased in remotely sensed observations. The need for high-resolution observations of rift propagation has been answered in part by deploying seismic arrays to continuously monitor the elastic wave emissions from rifts on short timescales (Bassis et al., 2005, Olinger et al., 2019). However, despite the promising results of rift seismology, the logistical complexity and hazard of field campaigns in active areas of ice shelf deformation mean that only a handful of seismic arrays have been deployed near rifts. Furthermore, seismic studies have been unable to capture any instances of truly rapid rifting despite evidence that such events do occur (Banwell et al., 2007).

In this study, we analyze rift propagation at Pine Island Glacier Ice Shelf (PIG), a fast-flowing ice shelf in West Antarctica that was the single largest Antarctic contributor to sea level rise in the period 1979–2017 (Rignot et al., 2019). Since 1992, tabular icebergs have calved from PIG every 2–6 years along rifts that propagated from the northern and southern shear margins, maintaining a relatively consistent ice front position and orientation (Arndt et al., 2018). In 2015, calving occurred along a rift that initiated in the ice shelf's center for the first time, resulting in substantial ice front retreat and reorientation (Jeong et al., 2016) that has continued to the present. Before this change in ice front geometry, the last calving event occurred in 2013 along a rift that propagated from the northern shear margin across the ice shelf, hereinafter referred to as R2011 for the year of its initiation. Here, we overcome the perennial limitation of studies of calving processes –namely, a lack of in situ observations (Benn et al., 2007)– and present the first-known near-field seismic observations of a large ice shelf rift propagation event.

## 2 Observations

### 2.1. Identifying rift propagation in SAR data

We manually examine synthetic aperture radar data collected by the TerraSAR-X (TSX) satellite (Pitz, & Miller, 2010) to identify an episode of rapid propagation during the rifting that preceded the 2013 calving event. One of the northern shear margin fractures, hereinafter referred to as R2012, propagated across the ice shelf and connected with R2011. TSX data from May 8, 2012 04:04 UTC show the PIG ice shelf before the episode of rift extension (Fig. 1A). The rift R2011 spanned 33.8 km across the ice shelf from the northern shear margin, and a band of ~20 shorter parallel fractures spanned ~5 km from the northern shear margin. The data show no major rifts besides R2011. TSX data from May 11, 2012 03:13 show the PIG ice shelf after the episode of rift extension (Fig. 1B), providing a three-day time window around the episode of rift extension. A high-resolution digital elevation model of PIG (Shean et al., 2019) shows that the tip of R2012 was located in a basal trough before propagation, consistent with previous observations that suggest basal channels strongly influence rift propagation on PIG and other ice shelves (Alley et al., 2019; Dow et al., 2018).

## 2.2. Identifying rift propagation in seismic data

We identify the rift seismic signal within data recorded by three Nanometrics Trillium 120 seismometers deployed on the PIG ice shelf and three Nanometrics Trillium 240 seismometers deployed across West Antarctica (Holland & Bindenschadler, 2012). Seismic data recorded in the time window established by TSX data contains a single notable signal, recorded on May 9, 2012 at 18:03 (Fig. 1C). We hypothesize that this signal, the largest amplitude signal within the three-day window, was generated by the extension of R2012 observed in TSX data. We use the cumulative amplitude distribution of the signal to estimate a duration of 2.09 hours, longer in duration than all other signals in the time window by an order of magnitude. The May 9 event has a peak vertical ground velocity of 0.234 mm/s and peak vertical ground displacement of 0.195 mm at a distance of 12 km and uniquely contains significant energy at periods up to 1000 s. The sensitivity of the Trillium 120 seismometer is reduced below its natural period of 120 s, suggesting that the amplitudes recorded between periods of 120 s and 1000 s may underestimate actual ice shelf velocities at those periods. Between 1000 s and 1 s periods, the signal exhibits high-frequency-first dispersion characteristic of flexural gravity (FG) waves (Fig. 1D), a wave type that propagates as a coupled beam flexural and ocean surface wave (Abrahams et al., 2022; Press & Ewing, 1951; Sergienko, 2017; Squire, 2007). At frequencies above 1 Hz, the signal consists of body and surface waves that gradually increase in amplitude before abruptly decaying after 302 s (Fig. 1E). These higher-frequency phases are also recorded by regional POLENET stations DNTW, THUR, and UPTW, respectively located 250, 294, and 360 km from PIG.

## 3 Methods

### 3.1. Mapping rift extent

We employ a semi-automated scheme to identify the extent of R2012 before and after propagation. We use TSX data from May 5, 2012 03:22:11 and May 11, 2012 03:13:39, which were captured from similar incidence angles and span the same spatial extent. To remove the effect of ice shelf advection, we cross-correlate windows containing the rift tip from each TSX data to obtain the optimal shift between the two data. We then use the computed shift to align the two data. To measure the increase in length of R2012, we normalize the data from May 5 and May 11 such that pixels with values close to 1 correspond to dark features like rifts. We then subtract the pre-extension image from the post-extension image to remove all features constant between May 5 and May 11, including shear margin fractures and R2011. We extract the largest 1-valued region from the differenced data, corresponding to the increase in the area of R2012. We then skeletonize the binary rift image, measure the length of the skeleton's main branch in pixels, and multiply by the TSX data's pixel size to extract the increase in length between May 5 and May 11. Finally, we sum the binary rift image to obtain the area of the rift in pixels, multiply by the TSX data's pixel size to obtain the rift area in square meters, then divide by the increase in length of R2012 to obtain an estimate of the average rift width. We estimate an increase in length of 10473.26 meters and a final average width of 132 meters. We follow the same procedure to estimate the initial length and width of R2012, finding an initial length of 3889.94 meters and an initial width of 91.25 meters.

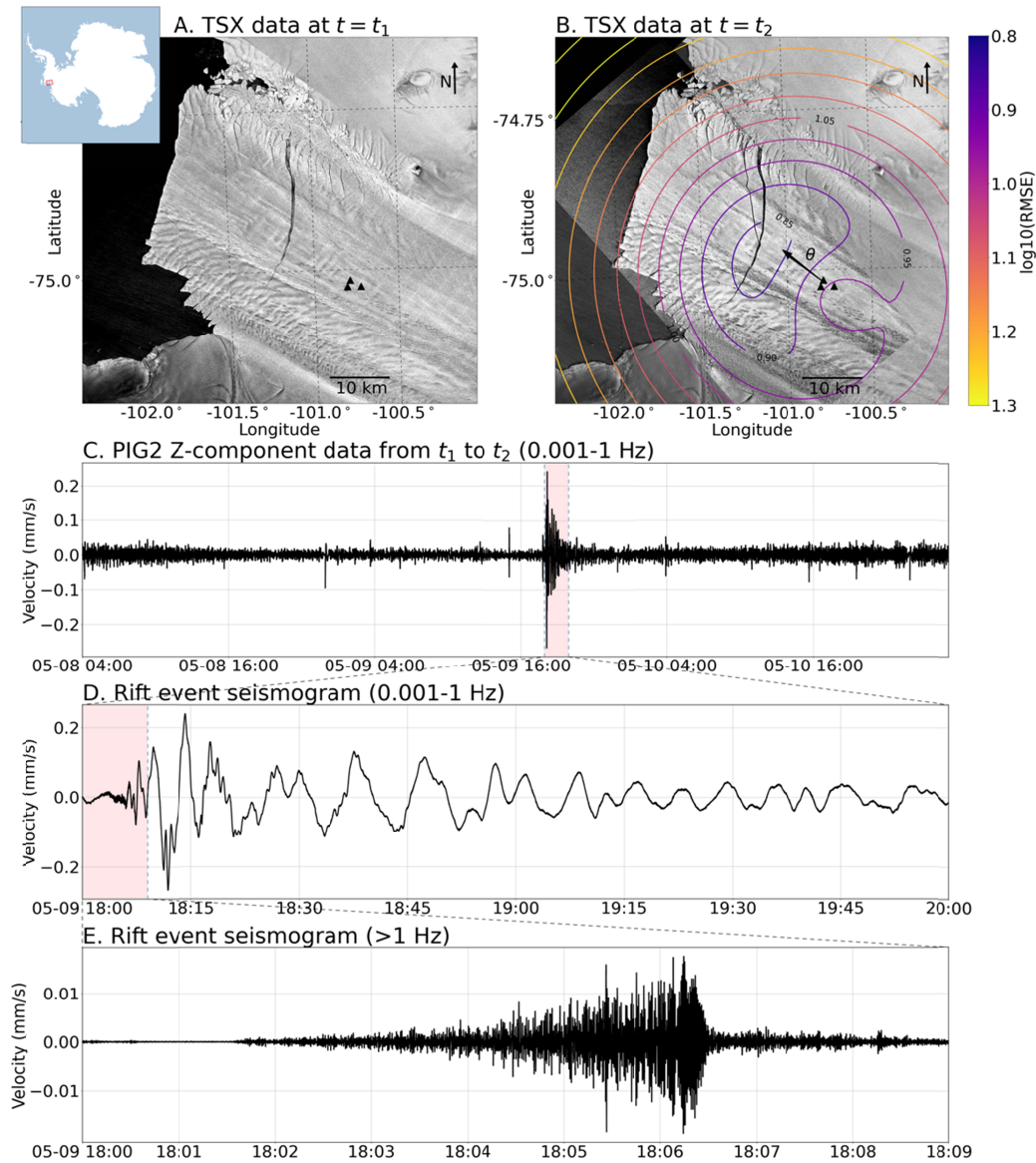


**Fig. 1. TSX and seismic data surrounding 10.5 km of rift propagation.** All seismic data are vertical velocity seismograms recorded by station PIG2. (A) TSX data from May 8, 2012 04:04 ( $t_1$ ) before propagation of R2012. Black triangles show on-ice seismic stations. The inset shows the location of PIG2 within Antarctica. (B) TSX data from May 11, 2012 03:13 ( $t_2$ ) after propagation of R2012. Contours show the logarithm of root mean squared error (RMSE) in arrival time residuals from a grid search of possible locations of the May 9 signal computed using on-ice seismic stations and regionally-deployed seismic stations (not shown). Arrow denoted by  $\theta$  shows backazimuth computed using the polarization of seismic waves recorded by on-ice seismic stations. (C) Seismogram spanning the time window between TSX data. The rift event signal is highlighted in pink. (D) Seismogram of rift event filtered between 0.001 Hz and 1 Hz. In this frequency band, the signal is dominated by flexural gravity (FG) waves. Resonance of ice shelf modes results in an event duration on the order of hours. (E) Seismogram of rift event filtered above 1 Hz. In this frequency band, the signal is dominated by P waves and surface waves. The abrupt decay of the rift event signal 302 s after the onset of the event indicates the conclusion of rift propagation.

### 3.2. Seismic location

To locate the candidate rift event, we first employ a grid search algorithm using arrival times at locally and regionally-deployed stations. To obtain the relative arrival times of high-frequency waves (1.5-5 Hz) at each station, we cross-correlate the filtered signal recorded at PIG2, the closest station to R2012, with the filtered signal recorded at each other station. Next, we calculate the velocity of the waves recorded at each station by dividing the known distance between PIG2 and each station by the difference between the arrival time at PIG2 and each station. We carry out this procedure using vertical, north-south, and east-west component data recorded at stations PIG2, PIG4, PIG5, THUR, BEAR, DNTW, and UPTW. We then conduct the grid search by iterating through possible origin times and spatial locations and computing the expected arrival time at each station using the previously-estimated phase velocity. We calculate the root mean square error (RMSE) between the observed and expected arrival times for all components and stations, giving a single estimate of the misfit in arrival times across the array. We then calculate RMSE for each possible origin time and for every spatial point in a regular grid to obtain a map of error. The event location is finally determined by identifying the spatial point and origin time that correspond to the lowest RMSE.

To further constrain the source location, we use the polarization direction of horizontal waves recorded at on-ice stations PIG2, PIG4, and PIG5 to compute an epicentral back-azimuth. By performing the principal component analysis (PCA) on the east-west and north-south seismograms, we obtain the PCA first component, a vector corresponding to the direction along which the majority of the variation in the data occurs. We infer the polarization direction from the PCA first component, which corresponds to one of two possible propagation directions separated by 180 degrees. To resolve this 180-degree ambiguity, we identify the two stations farthest from the array centroid in both possible directions of propagation, which are expected to record the first arrivals for incoming plane waves from either propagation direction. We then adjust the sign of the PCA first component to match the propagation direction whose predicted first arrival agrees with the observed first arrival. We repeat this procedure using data recorded at each station and sum the PCA first component vectors from each station to obtain an average propagation direction. Finally, we retrieve a back-azimuth by taking the arctangent of the quotient of the two elements of the PCA component vector. We repeat the entire procedure for each 50 s time window in the event, resulting in a distribution of back-azimuths calculated for each time window within the event. We obtain a single event back-azimuth by taking the circular mean of the back-azimuths calculated from each time window, with the back-azimuth from each time window weighted by the norm of the summed PCA components across the array for that window.

### 3.3. Ocean-coupled fracture modeling

We model the coupled ocean-rift system using simple linear elastic fracture mechanics and fluid dynamics. Given the relatively limited observations of rift growth, we have pursued a simplified model. Modeling efforts with increased complexity inherently lead to a greater number of model variables that, in our case, cannot be compared to observations. In the absence of more detailed observations, added complexity offers little benefit compared to the simplified case.

We utilize a coordinate system where the ice shelf base has a vertical position of 0, the ice front has a position of 0 in the y-direction, and the back of the rift has a position of 0 in the x-

direction. Our modeling employs the following equations, which are derived or discussed in more detail in Supporting Information Text S2-S7.

The conservation of water mass in the rift (derived in Text S2) is:

$$u = \frac{1}{LH_c} \left[ wL \frac{d\eta}{dt} + w\eta \frac{dL}{dt} + L\eta \frac{dw}{dt} \right] \quad (1)$$

where  $\eta$  is the water level within the rift,  $w$  is the width of the rift, and  $u$  is the water flow rate,  $H_c$  is the subshelf cavity height (assumed uniform), and  $L$  is the rift length. Although spatial variations in  $H_c$  exist (Muto et al, 2016; Shean et al., 2019) and could play a role in higher order dynamics, we assume uniformity in order to describe only the most basic features of ocean-rift coupling.

We write the conservation of fluid momentum (derived in Text S3-S4) as:

$$L_c \frac{du}{dt} + (H_w - H_c) \frac{d\eta^2}{dt^2} = g(H_w - H_c - \eta) \quad (2)$$

where  $L_c$  is the horizontal position of the rift and  $H_w$  is the height from the ice shelf base to the hydrostatic water line.

The depth integrated rift extensional stress (discussed in Text S5) is:

$$\sigma = R_{xx} + \frac{\rho_w g \eta^2}{2H_i} - \frac{\rho_i g H_i}{2}$$

The rift width (discussed in Text S6) is:  $w = w_0 + \frac{\pi\sigma}{4\mu^*} L$

where  $\mu^* = \mu/(1 - \nu)$ ,  $\mu$  is the shear modulus, and  $\nu$  is Poisson's ratio.

The rift tip equation of motion (discussed in Text S7) is:

$$\frac{dL}{dt} \approx c_r \left( 1 - \frac{K_c^2}{K_I^2} \right) \quad (3)$$

where  $K_I$  is the stress intensity factor experienced by the rift and  $K_c$  is the fracture toughness of ice.

We seek to solve the system of ordinary differential equations (ODEs) defined by Eq. 1, Eq. 2, and Eq. 3 for  $L$  and  $\eta$ . We utilize a widely-available class of ODE solvers that handle systems of equations with the form,

$$x' = f(x, x')$$

i.e. systems that only have a dependence on the first derivatives  $x'$  of the state vector  $x$ . Through algebraic manipulation, we write Eq. 1, Eq. 2, and Eq. 3 in this form. This requires introducing a

variable  $\chi = \eta'$  so the 2nd derivative  $\eta''$  can be written as a first derivative. This also requires us to obtain an equation for  $\chi''$ . We accomplish this by rearranging Eq. 2, analytically computing all the necessary derivative terms, and substituting. This process yields a set of equations written in a convenient way for numerical solutions. However, the equations in the previous sections are more physically interpretable, so the forms used in obtaining a numerical solution are not reproduced here. In our simulations, we first compute the ice shelf extensional stress  $R_{xx}$  necessary for a fracture of the prescribed initial geometry to experience a stress intensity factor that barely exceeds the fracture toughness of ice. We then use compute the stress and stress intensity factors corresponding to  $R_{xx}$  assuming an initial steady-state water surface height of  $\eta = H_i \rho_w / \rho_i$ . This initiates fracture propagation at a rate determined by Eq. 3.  $R_{xx}$  is held fixed through the simulation, and the stress applied to the rift evolves through time as  $\eta$  changes.

## 4 Results

### 4.1. Origin of observed seismic signal

A previous study of fracture at PIG identified FG waves generated by gradual propagation of R2011 (Olinger et al., 2022), suggesting the extension of R2012 is a reasonable source for the May 9 event. In addition to rift propagation, FG waves on ice shelves are generated by incoming ocean waves (Chen et al., 2020). However, ocean wave sources cannot account for seismic phases recorded by regional stations hundreds of kilometers away, and we therefore conclude that incoming ocean waves must not have generated the rift signal. Additionally, the spectrum of the May 9 event is markedly different than teleseismic earthquake spectra recorded by the same instrument (Fig. S1), and we conclude that teleseismic waves must not have generated the May 9 event signal. A grid-search inversion of arrival times at locally and regionally-deployed seismic stations finds its lowest-error region where R2012 connects to R2011 (Fig. 1B), further supporting the hypothesis that the extension of R2012 generated the May 9 event. The polarization of waves recorded at locally-deployed stations corresponds to a back-azimuth of  $308.1 \pm 6.2$  degrees (Fig. 1B), in agreement with the back-azimuth of R2012, confirming that the recorded waves propagated to the local seismic stations from the direction of R2012. Because the best-fit event location coincides with R2012 and because both teleseismic and ocean wave sources are inconsistent with the seismic observations, we conclude that the May 9, 18:03 event was the seismic signal generated by the extension of R2012.

### 4.2. Rate of observed rift propagation

To understand the dynamics of the observed rift propagation, we estimate the rupture velocity using the duration of radiated body and surface waves and the increase in length estimated from TSX data. Radiated body and surface waves gradually crescendo, consistent with an accelerating rupture or a seismic source that moves progressively closer to the seismometers (our limited station geometry precludes distinguishing between these two scenarios). Seismic waves then abruptly stop after 302 s (Fig. 1E), indicating the conclusion of propagation when R2012 collided with R2011. Such a “stopping phase” is highly unusual; stopping phases are not typically observed in tectonic earthquakes, for example. We thus infer that the observed 10.5 km of rift extension occurred over 302 s, corresponding to an average rupture velocity of 34.8 m/s. To the best of our knowledge, this is the fastest rift propagation speed ever observed. R2012 extended over a duration of time two orders of magnitude below the Maxwell time of ice, which is around 11 hours (Ultee et al., 2020), supporting the hypothesis that the observed rift extension



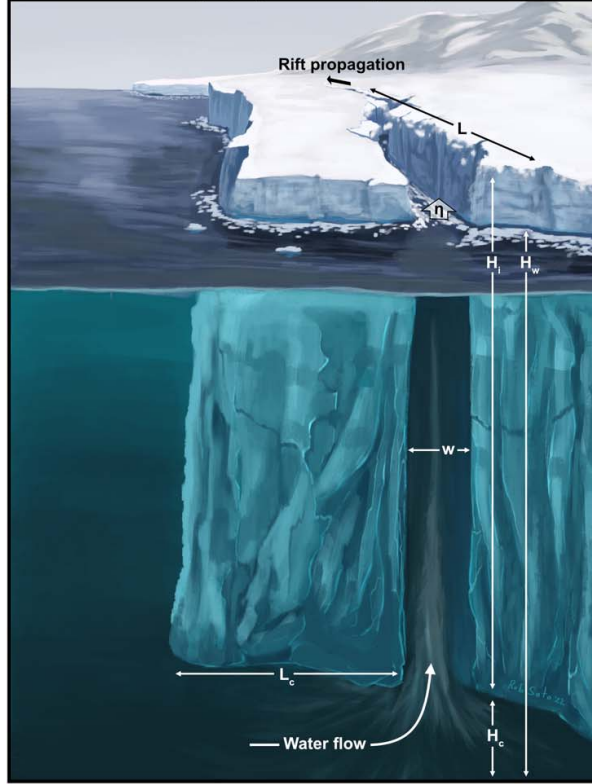
occurred through dynamic brittle fracturing. However, elastodynamic theory predicts opening mode fracture propagation at rates approaching the Rayleigh wave speed of the fracturing material (Freund, 1990), which is between 1500 and 2000 m/s in the ice (Kim et al, 2010). Why, then, did R2012 propagate two orders of magnitude below the Rayleigh wave speed?

### 4.3. Modeled ocean-coupled rift dynamics

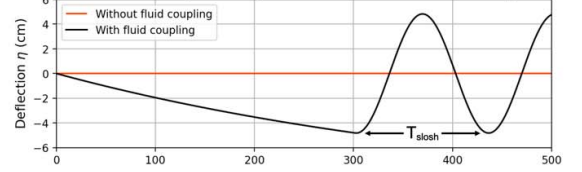
We hypothesize that coupling between rift propagation and water flow within the rift explains rupture at a small fraction of the Rayleigh wave speed. To test the hypothesis, we develop a simple model of rift propagation that couples brittle fracture and water flow. The rift is represented by a sharp fracture in a linear elastic plate subject to uniform far-field tension. Water flows through the subshelf cavity into the rift is represented using the unsteady Bernoulli flow approximation. To initiate rift extension, we apply the stress required for a fracture of a chosen initial geometry to experience a stress intensity factor that just exceeds the fracture toughness of ice. As the rift propagates, the total volume within the rift increases, and water rushes in to fill the rift. However, water flow into the rift is not rapid enough to maintain the hydrostatic water line, causing a reduction in the average water height within the rift and a decrease in the depth-integrated water pressure acting to open the rift (Fig. 2A). The lower water pressure reduces the total resolved stress that drives rift opening, and in turn, limits the rate of propagation. This effect results in a far lower rupture velocity than predicted for a rift with a static water height. If propagation stops abruptly, fluid inflow continues due to inertia and overshoots the steady-state water line, resulting in simple harmonic oscillations about the steady-state water line (e.g., Fig. 2B after  $t=300$  s). These simple harmonic oscillations occur at the sloshing period,  $T_{slosh} = 2\pi\sqrt{M/g}$ , where  $M = L_c w / H_c + H_w - H_c$  is a measure of the effective cross-sectional area of water being transported,  $L_c$  is the distance from the rift to the ice front,  $w$  is the width of the rift,  $H_c$  is the distance from the seafloor to the base of the ice shelf, and  $H_w$  is the distance from the seafloor to the water surface. The sensitivity of modeled rupture velocities to ice shelf geometry and  $R_{xx}$  are shown in the Supporting Information (Figs. S2-S4).

To test whether the proposed model can explain the observed propagation rate of R2012, we model R2012 using an initial length of 3.9 km and an initial width of 90 m that were measured from TSX data. We assume that the ice shelf has a uniform ice thickness of 400 m, estimated from a high-resolution digital elevation model of PIG from 2012 (Shean et al., 2019), and a uniform water depth of 840 m, estimated from a gravity-derived model of Pine Island Bay bathymetry (Muto et al., 2016). The rift is subjected to a spatially-uniform extensional stress  $R_{xx}$ . The magnitude of  $R_{xx}$  is obtained by computing the stress required for a rift with the measured initial geometry to begin unstable propagation and identifying the additional stress needed for the rift to grow 10.5 km in 302 s. The modeled rift begins propagating when an extensional stress of approximately 161 kPa is applied. This is consistent with a previous estimate which found that the central region of PIG ice shelf had a mean  $R_{xx}$  of approximately 124 kPa (Lai et al., 2020) (Fig. S5). Once propagation begins, the rift propagates 10.5 km over a duration of 302 s at an average rate of 34.8 m/s (Fig. 2E). The predicted rupture velocity of 34.8 m/s agrees with the observed rupture velocity, strongly supporting the hypothesis that coupling between rift propagation and water flow limited the observed rupture velocity to a small fraction of the Rayleigh wave speed. Without fluid coupling, a fracture of the same initial geometry subjected to the same magnitude of stress reaches 99% of the Rayleigh wave speed in 302 s, highlighting how significantly the mechanism we propose influences the dynamics of rift propagation.

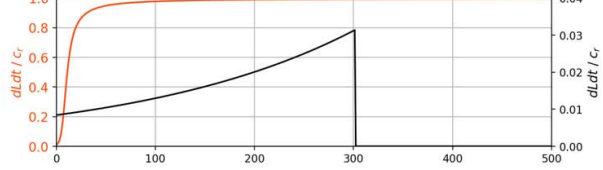
A. Schematic of rift propagation and hydrodynamics



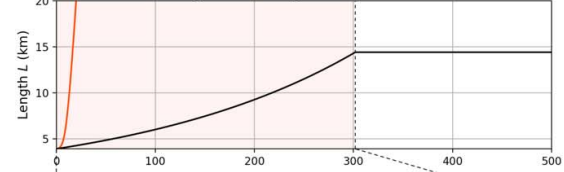
B. Deflection  $\eta$  from hydrostatic water level through time



C. Propagation rate  $dL/dt$  through time



D. Fracture length  $L$  through time



E. Fracture length  $L$  through time over 302 s

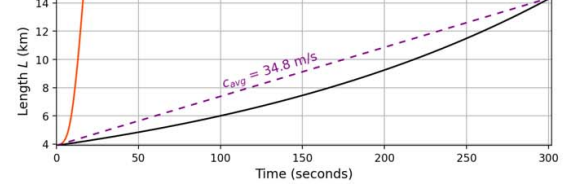


**Fig. 2. Ocean-coupled model of rift propagation.** In all panels, black curves show a rift coupled to hydrodynamics, and orange curves show a rift uncoupled to hydrodynamics. (A) Illustration of the proposed mechanism for rift propagation at a small fraction of the Rayleigh wave speed ( $c_r$ ). (B) Modeled perturbation from hydrostatic water level during rift propagation. In the coupled case, the water level initially decreases because water flow into the rift is not fast enough to maintain the hydrostatic water level. Once propagation concludes, flow overshoots the hydrostatic water level and oscillates at the sloshing period  $T_{slosh}$ . In the uncoupled case, the water level in the rift does not change. (C) Modeled rift propagation rate through time. In the coupled case, decreasing water pressure limits propagation to a small fraction of  $c_r$ . In the uncoupled case, propagation approaches  $c_r$  rapidly. (D) Modeled rift length through time for 500 s of rift propagation. (E) Modeled rift length through time for 302 s of rift propagation. In the coupled case, the rift length increases by 10.5 km at an average rate of 34.8 m/s, in agreement with the observed propagation rate of R2012. In the uncoupled case, the rift propagates at a rate far exceeding the observation.

## 5 Discussion

Our observations suggest that ice shelf rift propagation occurs more rapidly than previously known (Walker et al., 2013). An immediate conclusion from this observation is that the timescale of fracture at R2012 is well within the regime of brittle fracture. Yet our observations and modeling show that the rift propagation of R2012 was not purely governed by the laws of linear elastic fracture mechanics because rift propagation was slowed down by interaction with the ocean. Several aspects of R2012 warrant further discussion.

### 5.1. Rapid rifting and ice shelf stability

Rapid rift propagation represents a possible mechanism of sudden ice front retreat or ice shelf collapse. While previous observations of rift propagation have overwhelmingly captured gradual or episodic propagation (Bassis et al., 2005; Bassis et al., 2007; Jeong et al., 2016; Walker et al., 2013), we show that rift propagation on the order of 10 km can occur in a matter of minutes. It is unknown whether this represents a rare class of rift behavior or a relatively common class of rift behavior that has remained undetected until now due to the temporal aliasing of remotely-sensed observations and a scarcity of ice shelf seismic deployments. As PIG continues to accelerate, elevated stresses and shear margin weakening are expected to enhance rift propagation (Lhermitte et al., 2020; Lipovsky, 2020), which can, in turn, lead to ice front retreat, buttressing loss and further acceleration (Joughin et al., 2021). Our observations suggest that such feedback at PIG and other unstable ice shelves across Antarctica may progress more rapidly than anticipated.

### 5.2. Flexural gravity waves generated by rift propagation

We use the wave impedance tensor (Lipovsky, 2018) to compute the maximum flexural stresses carried by FG waves recorded at each local station and estimate a mean flexural stress of 3.26 kPa, consistent with typical ocean wave-induced flexural stresses on Ross Ice Shelf (Aster et al., 2021; Lipovsky, 2018) and potentially large enough to trigger additional fracturing within the ice shelf. However, PIG typically experiences a lower degree of ocean wave excitation than Ross Ice Shelf (Chen et al., 2018), so FG waves generated by rift propagation may exert a greater influence than ocean waves on the stability of fractures on PIG.

The 600 s dominant period of the recorded FG waves is between the gravest ice shelf resonance period ( $\sim 1600$  s) and the sloshing period ( $T_{slosh} \sim 100$  s), suggesting that both of these processes are involved in generating the observed FG wave field. Accounting for radiative losses at the ice front using the relevant reflection coefficient (Abrahams et al., 2022) results in an underestimate of the e-folding duration (i.e., time to achieve decay by a factor of  $1/e$ ) of the wave field as 16.7 minutes. However, it takes 38.2 minutes for recorded FG waves to decay by a factor of  $1/e$ . The e-folding duration is therefore plausibly attributed to wave generation by water sloshing within the rift that continues after rift propagation ceases (see, for example, Fig. 2B).

### 5.3. Mixing induced by rapid rifting

We infer that large rift propagation events induce diapycnal mixing in the subshelf cavity, i.e., vertical flow in the presence of horizontal density surfaces (Holland et al., 2019; Jacobs et al., 2011). In the context of smaller-scale calving, Meredith et al. (2022) recently observed such mixing following a calving event with potential energy change  $(0.6\text{--}2.4) \times 10^{12}$  J. At R2012, we

estimate the potential energy change  $1.2 \times 10^{12}$  J over the five-minute duration of rift propagation and  $879 \times 10^{12}$  J over the subsequent several days of rift opening (Text S7). Whether the internal tsunami mixing mechanism proposed by Meredith et al. (2022) is able to operate at the timescale of the longer-duration potential energy change depends on the water column stratification through the buoyancy oscillation frequency (Gill, 1982), information which is not available during the time of R2012. However, for both cases, the scale of energy associated with vertical diapycnal flow implies significant subshelf mixing during rift growth, contrary to earlier reports (Meredith et al., 2022).

During the several minutes of rift propagation, we calculate the vertical water volume flux to be at least  $2300 \text{ m}^3/\text{s}$ . PIG is known to have a complex basal topography with pervasive longitudinal basal crevasses that penetrate as much as 30% of the ice thickness (Vaughan et al., 2012) and that are perpendicular to the propagation direction of the rift. On other ice shelves, such features have been shown to guide the direction of rift propagation (De Rydt et al., 2018). Such basal crevasses do not play a significant role in our simplified model since we do not attempt to model the rift propagation path. If the R2012 rift did follow a basal crevasse with a height of 30% the ice thickness, this would reduce our vertical flow estimate by the same percentage.

Rifting-induced mixing suggests the existence of positive feedback between these processes. Despite significant thermocline variability, sub-shelf waters in the vicinity of the rift R2012 are deep enough to consistently reach the depth of warm circumpolar deep waters (Christianson et al., 2016). Rift propagation in this setting may therefore elevate isothermal contours and cause warming of the ice–ocean interface. Localized and repeated rift propagation in areas like the northern shear margin of PIG (Fig. 1A) may then initiate feedback wherein rift propagation induces mixing and localized melting that contributes to marginal weakening (Lipovsky, 2020) and the formation of basal melt channels (Alley et al., 2019; Dow et al., 2018), thereby promoting further rift propagation.

## 6 Conclusions

We conclude that rifts can propagate rapidly through brittle fracture and that the ocean exerts a profound influence on rift propagation. Whereas the largest fracturing events on land, i.e., tectonic earthquakes, are ultimately inertially limited (Dunham, 2007), our observations and models imply that the largest fracturing events in ice, e.g., ice shelf rift propagation events, are ultimately hydrodynamically limited. We therefore add to the body of literature documenting diverse ice-ocean interactions and demonstrate that extreme ice shelf sensitivity to ocean conditions extends to the fine-scale dynamics of rift propagation.

**Acknowledgments:** The facilities of IRIS Data Services and IRIS Data Management Center were used for access to waveforms, metadata, and/or derived products used in this study. IRIS Data Services are funded through the Seismological Facilities for the Advancement of Geoscience (SAGE) Award of the National Science Foundation under Cooperative Support Agreement EAR-1851048. Seismic instruments were provided by the Incorporated Research Institutions for Seismology (IRIS) through the PASSCAL Instrument Center at New Mexico Tech. The facilities of the IRIS Consortium are supported by the National Science Foundation's Seismological Facilities for the Advancement of Geoscience (SAGE) Award under Cooperative Support Agreement EAR-1851048. TSX data was provided courtesy of the German Aerospace Center (DLR) through proposal GEO3838. Rob Soto was contracted by the authors for the creation of the model schematic in Fig. 2A. The work published here was funded by National Science Foundation Office of Polar Programs award 1853896, awarded to BPL. SDO was also supported by startup funds of MAD at Harvard University in the Department of Earth and Planetary Sciences. The authors declare that they have no competing interests.

**Open Research:** The seismic data set was collected by Holland and Bindshadler (2012) and is available through IRIS (Holland & Bindshadler, 2012) with the DOI [https://doi.org/10.7914/sn/xc\\_2012](https://doi.org/10.7914/sn/xc_2012). TerraSAR-X data used in this study are available to registered users for research purposes through the DLR EOWEB GeoPortal (<https://eoweb.dlr.de/egp/>) and can be located using the data IDs provided in Table S1. Codes necessary to reproduce the data analysis and modeling are available at the GitHub repository [https://github.com/stepholinger/olinger\\_et\\_al\\_2023](https://github.com/stepholinger/olinger_et_al_2023) and hosted on Zenodo (Olinger, 2023) with the DOI <https://doi.org/10.5281/zenodo.7466085>.

## References

1. Abrahams, L. S., Mierzejewski, J. E., & Dunham, E. M. (2022). Ocean Surface Gravity Wave Excitation of Flexural Gravity and Extensional Lamb Waves in Ice Shelves. *EarthArXiv*. <https://doi.org/10.31223/X5GW60>
2. Aki, K., & Richards, P. G. (2002). *Quantitative seismology*. University science books.
3. Alley, K. E., Scambos, T. A., Alley, R. B., & Holschuh, N. (2019). Troughs developed in ice-stream shear margins precondition ice shelves for ocean-driven breakup. *Science Advances*, 5(10), eaax2215. <https://doi.org/10.1126/sciadv.aax2215>
4. Arndt, J. E., Larter, R. D., Friedl, P., Gohl, K., Høppner, K., & others. (2018). Bathymetric controls on calving processes at Pine Island Glacier. *The Cryosphere*, 12(6), 2039–2050.
5. Aster, R. C., Lipovsky, B. P., Cole, H. M., Bromirski, P. D., Gerstoft, P., Nyblade, A., Wiens, D. A., & Stephen, R. (2021). Swell-Triggered Seismicity at the Near-Front Damage Zone of the Ross Ice Shelf. *Seismological Research Letters*, 92(5), 2768–2792. <https://doi.org/10.1785/0220200478>
6. Banwell, A. F., MacAyeal, D. R., & Sergienko, O. V. (2013). Breakup of the Larsen B Ice Shelf triggered by chain reaction drainage of supraglacial lakes. *Geophysical Research Letters*, 40(22), 5872–5876.
7. Banwell, A. F., Willis, I. C., Macdonald, G. J., Goodsell, B., Mayer, D. P., Powell, A., & Macayeal, D. R. (2017). Calving and rifting on the McMurdo Ice Shelf, Antarctica. *Annals of Glaciology*, 58(75pt1), 78–87. <https://doi.org/10.1017/aog.2017.12>
8. Bassis, J., Berg, B., Crawford, A., & Benn, D. (2021). Transition to marine ice cliff instability controlled by ice thickness gradients and velocity. *Science*, 372(6548), 1342–1344.
9. Bassis, J. N., Coleman, R., Fricker, H. A., & Minster, J. B. (2005). Episodic propagation of a rift on the Amery Ice Shelf, East Antarctica. *Geophysical Research Letters*, 32(6). <https://doi.org/10.1029/2004GL022048>
10. Bassis, J. N., Fricker, H. A., Coleman, R., Bock, Y., Behrens, J., Darnell, D., Okal, M., & Minster, J.-B. (2007). Seismicity and deformation associated with ice-shelf rift propagation. *Journal of Glaciology*, 53(183), 523–536. <https://doi.org/10.3189/002214307784409207>
11. Benn, D. I., Warren, C. R., & Mottram, R. H. (2007). Calving processes and the dynamics of calving glaciers. *Earth-Science Reviews*, 82(3–4), 143–179.
12. Borstad, C., Khazendar, A., Larour, E., Morlighem, M., Rignot, E., Schodlok, M., & Seroussi, H. (2012). A damage mechanics assessment of the Larsen B ice shelf prior to collapse: Toward a physically-based calving law. *Geophysical Research Letters*, 39(18).
13. Chen, Z., Bromirski, P. D., Gerstoft, P., Stephen, R. A., Wiens, D. A., Aster, R. C., & Nyblade, A. A. (2018). Ocean-excited plate waves in the Ross and Pine Island Glacier ice shelves. *Journal of Glaciology*, 64(247), 730–744. <https://doi.org/10.1017/jog.2018.66>

- 475 14. Christianson, K., Bushuk, M., Dutrieux, P., Parizek, B. R., Joughin, I. R., Alley, R. B.,  
 476 Shean, D. E., Abrahamsen, E. P., Anandakrishnan, S., Heywood, K. J., Kim, T.-W., Lee, S.  
 477 H., Nicholls, K., Stanton, T., Truffer, M., Webber, B. G. M., Jenkins, A., Jacobs, S.,  
 478 Bindschadler, R., & Holland, D. M. (2016). Sensitivity of Pine Island Glacier to observed  
 479 ocean forcing. *Geophysical Research Letters*, 43(20), 10,817–10,825.  
 480 <https://doi.org/10.1002/2016GL070500>
- 481 15. Clerc, F., Minchew, B. M., & Behn, M. D. (2019). Marine ice cliff instability mitigated by  
 482 slow removal of ice shelves. *Geophysical Research Letters*, 46(21), 12108–12116.
- 483 16. David Holland & Robert Bindschadler. (2012). *Observing Pine Island Glacier (PIG) ice*  
 484 *shelf deformation and fracture using a GPS and Seismic Network*. International Federation of  
 485 Digital Seismograph Networks. [https://doi.org/10.7914/SN/XC\\_2012](https://doi.org/10.7914/SN/XC_2012)
- 486 17. De Rydt, J., Gudmundsson, G. H., Nagler, T., Wuite, J., & King, E. C. (2018). Recent rift  
 487 formation and impact on the structural integrity of the Brunt Ice Shelf, East Antarctica. *The*  
 488 *Cryosphere*, 12(2), 505–520. <https://doi.org/10.5194/tc-12-505-2018>
- 489 18. DeConto, R. M., & Pollard, D. (2016). Contribution of Antarctica to past and future sea-level  
 490 rise. *Nature*, 531(7596), 591–597.
- 491 19. Dow, C. F., Lee, W. S., Greenbaum, J. S., Greene, C. A., Blankenship, D. D., Poinar, K.,  
 492 Forrest, A. L., Young, D. A., & Zappa, C. J. (2018). Basal channels drive active surface  
 493 hydrology and transverse ice shelf fracture. *Science Advances*, 4(6), eaao7212.  
 494 <https://doi.org/10.1126/sciadv.aao7212>
- 495 20. Dunham, E. M. (2007). Conditions governing the occurrence of supershear ruptures under  
 496 slip-weakening friction. *Journal of Geophysical Research: Solid Earth*, 112(B7).
- 497 21. Freund, L. B. (1990). *Dynamic Fracture Mechanics*. Cambridge University Press.  
 498 <https://doi.org/10.1017/CBO9780511546761>
- 499 22. Fürst, J. J., Durand, G., Gillet-Chaulet, F., Tavard, L., Rankl, M., Braun, M., & Gagliardini,  
 500 O. (2016). The safety band of Antarctic ice shelves. *Nature Climate Change*, 6(5), 479–482.
- 501 23. Greene, C. A., Gardner, A. S., Schlegel, N.-J., & Fraser, A. D. (2022). Antarctic calving loss  
 502 rivals ice-shelf thinning. *Nature*, 609(7929), 948–953.
- 503 24. Holland, P. R., Bracegirdle, T. J., Dutrieux, P., Jenkins, A., & Steig, E. J. (2019). West  
 504 Antarctic ice loss influenced by internal climate variability and anthropogenic forcing.  
 505 *Nature Geoscience*, 12(9), 718–724.
- 506 25. Hughes, T. J. (1981). The weak underbelly of the West Antarctic ice sheet. *Journal of*  
 507 *Glaciology*, 27(97), 518–525. <https://doi.org/10.3189/S002214300001159X>
- 508 26. Jacobs, S. S., Jenkins, A., Giulivi, C. F., & Dutrieux, P. (2011). Stronger ocean circulation  
 509 and increased melting under Pine Island Glacier ice shelf. *Nature Geoscience*, 4(8), 519–523.  
 510 <https://doi.org/10.1038/geo1188>

- 511 27. Jeong, S., Howat, I. M., & Bassis, J. N. (2016). Accelerated ice shelf rifted and retreat at  
512 Pine Island Glacier, West Antarctica. *Geophysical Research Letters*, 43(22), 11,720–11,725.  
513 <https://doi.org/10.1002/2016GL071360>
- 514 28. Joughin, I., Shapero, D., Smith, B., Dutrieux, P., & Barham, M. (2021). Ice-shelf retreat  
515 drives recent Pine Island Glacier speedup. *Science Advances*, 7(24), eabg3080
- 516 29. Kim, K., Lee, J., Hong, M., Hong, J., Jin, Y., & Shon, H. (2010). Seismic and radar  
517 investigations of Fourcade Glacier on King George Island, Antarctica. *Polar Research*, 29,  
518 298–310. <https://doi.org/10.1111/j.1751-8369.2010.00174.x>
- 519 30. Lai, C.-Y., Kingslake, J., Wearing, M. G., Chen, P.-H. C., Gentine, P., Li, H., Spergel, J. J.,  
520 & van Wessem, J. M. (2020). Vulnerability of Antarctica’s ice shelves to meltwater-driven  
521 fracture. *Nature*, 584(7822), 574–578.
- 522 31. Lhermitte, S., Sun, S., Shuman, C., Wouters, B., Pattyn, F., Wuite, J., Berthier, E., & Nagler,  
523 T. (2020). Damage accelerates ice shelf instability and mass loss in Amundsen Sea  
524 Embayment. *Proceedings of the National Academy of Sciences*, 117(40), 24735–24741.
- 525 32. Lipovsky, B. P. (2018). Ice Shelf Rift Propagation and the Mechanics of Wave-Induced  
526 Fracture. *Journal of Geophysical Research: Oceans*, 123(6), 4014–4033.  
527 <https://doi.org/10.1029/2017JC013664>
- 528 33. Lipovsky, B. P. (2020). Ice shelf rift propagation: Stability, three-dimensional effects, and  
529 the role of marginal weakening. *The Cryosphere*, 14(5), 1673–1683.  
530 <https://doi.org/10.5194/tc-14-1673-2020>
- 531 34. Meredith, M. P., Inall, M. E., Brearley, J. A., Ehmen, T., Sheen, K., Munday, D., Cook, A.,  
532 Retallick, K., Landeghem, K. V., Gerrish, L., Annett, A., Carvalho, F., Jones, R., Garabato,  
533 A. C. N., Bull, C. Y. S., Wallis, B. J., Hogg, A. E., & Scourse, J. (2022). Internal  
534 tsunamigenesis and ocean mixing driven by glacier calving in Antarctica. *Science Advances*,  
535 8(47), eadd0720. <https://doi.org/10.1126/sciadv.add0720>
- 536 35. Muto, A., Peters, L. E., Gohl, K., Sasgen, I., Alley, R. B., Anandakrishnan, S., & Riverman,  
537 K. L. (2016). Subglacial bathymetry and sediment distribution beneath Pine Island Glacier  
538 ice shelf modeled using aerogravity and in situ geophysical data: New results. *Earth and*  
539 *Planetary Science Letters*, 433, 63–75. <https://doi.org/10.1016/j.epsl.2015.10.037>
- 540 36. Olinger, S. D. (2023). solinger/olinger\_et\_al\_2023: December 21, 2022 Release (Version  
541 1.0) [Software]. Zenodo. <https://doi.org/10.5281/zenodo.7466085>
- 542 37. Olinger, S. D., Lipovsky, B. P., Denolle, M. A., & Crowell, B. W. (2022). Tracking the  
543 Cracking: A Holistic Analysis of Rapid Ice Shelf Fracture Using Seismology, Geodesy, and  
544 Satellite Imagery on the Pine Island Glacier Ice Shelf, West Antarctica. *Geophysical*  
545 *Research Letters*, 49(10), e2021GL097604. <https://doi.org/10.1029/2021GL097604>
- 546 38. Pattyn, F., Ritz, C., Hanna, E., Asay-Davis, X., DeConto, R., Durand, G., Favier, L.,  
547 Fettweis, X., Goelzer, H., Gollidge, N. R., Kuipers Munneke, P., Lenaerts, J. T. M.,  
548 Nowicki, S., Payne, A. J., Robinson, A., Seroussi, H., Trusel, L. D., & van den Broeke, M.



- (2018). The Greenland and Antarctic ice sheets under 1.5 °C global warming. *Nature Climate Change*, 8(12), 1053–1061. <https://doi.org/10.1038/s41558-018-0305-8>
39. Pitz, W., & Miller, D. (2010). The Terrasar-x satellite. *IEEE Transactions on Geoscience and Remote Sensing*, 48(2), 615–622. <https://doi.org/10.1109/TGRS.2009.2037432>
40. Press, F., & Ewing, M. (1951). Propagation of elastic waves in a floating ice sheet. *Eos, Transactions American Geophysical Union*, 32(5), 673–678.
41. Reese, R., Gudmundsson, G. H., Levermann, A., & Winkelmann, R. (2018). The far reach of ice-shelf thinning in Antarctica. *Nature Climate Change*, 8(1), 53–57.
42. Rignot, E., Casassa, G., Gogineni, P., Krabill, W., Rivera, A., & Thomas, R. (2004). Accelerated ice discharge from the Antarctic Peninsula following the collapse of Larsen B ice shelf. *Geophysical Research Letters*, 31(18).
43. Rignot, E., Mouginot, J., Scheuchl, B., Broeke, M. van den, Wessem, M. J. van, & Morlighem, M. (2019). Four decades of Antarctic Ice Sheet mass balance from 1979–2017. *Proceedings of the National Academy of Sciences*, 116(4), 1095–1103. <https://doi.org/10.1073/pnas.1812883116>
44. Robel, A. A., & Banwell, A. F. (2019). A speed limit on ice shelf collapse through hydrofracture. *Geophysical Research Letters*, 46(21), 12092–12100.
45. Scambos, T. A., Bohlander, J. A., Shuman, C. A., & Skvarca, P. (2004). Glacier acceleration and thinning after ice shelf collapse in the Larsen B embayment, Antarctica. *Geophysical Research Letters*, 31(18). <https://doi.org/10.1029/2004GL020670>
46. Segall, P. (2010). *Earthquake and Volcano Deformation*. Princeton University Press.
47. Sergienko, O. (2017). Behavior of flexural gravity waves on ice shelves: Application to the Ross Ice Shelf. *Journal of Geophysical Research: Oceans*, 122(8), 6147–6164.
48. Shean, D. E., Joughin, I. R., Dutrieux, P., Smith, B. E., & Berthier, E. (2019). Ice shelf basal melt rates from a high-resolution digital elevation model (DEM) record for Pine Island Glacier, Antarctica. *The Cryosphere*, 13(10), 2633–2656. <https://doi.org/10.5194/tc-13-2633-2019>
49. Squire, V. A. (2007). Of ocean waves and sea-ice revisited. *Cold Regions Science and Technology*, 49(2), 110–133.
50. Ultee, L., Meyer, C., & Minchew, B. (2020). Tensile strength of glacial ice deduced from observations of the 2015 eastern Skaftá cauldron collapse, Vatnajökull ice cap, Iceland. *Journal of Glaciology*, 66(260), 1024–1033. <https://doi.org/10.1017/jog.2020.65>
51. Vaughan, D. G., Corr, H. F. J., Bindshadler, R. A., Dutrieux, P., Gudmundsson, G. H., Jenkins, A., Newman, T., Vornberger, P., & Wingham, D. J. (2012). Subglacial melt channels and fracture in the floating part of Pine Island Glacier, Antarctica. *Journal of Geophysical Research: Earth Surface*, 117(F3). <https://doi.org/10.1029/2012JF002360>

585 52. Walker, C. C., Bassis, J. N., Fricker, H. A., & Czerwinski, R. J. (2013). Structural and  
586 environmental controls on Antarctic ice shelf rift propagation inferred from satellite  
587 monitoring. *Journal of Geophysical Research: Earth Surface*, 118(4), 2354–2364.  
588 <https://doi.org/10.1002/2013JF002742>